CCS Chemistry

RESEARCH ARTICLE

Received: Jan. 9, 2026 | Accepted: May 28, 2026 | Published: July 9, 2026

Conjugated Shape Persistent Heterocycle Macrocycles for Sacrificial Photocatalytic Hydrogen Evolution

Xinman Liu[1,2†], Hang Qu[2†], Chao Li[3†], Tao Liu[2,4], Ziheng Xiao[2], Shufan Feng[1], Qiang Zhu[2,4], Yu-Lin Lu[2], Jiayi Zhang[1], Zhiwu Yu[1], Teng-Teng Chen[3], Weiwei Zhang[1*], Charlotte E. Boott[2*], Jianli Hua[1*], He Tian[1] & Andrew I. Cooper[2,4*]

[1]*Key Laboratory for Advanced Materials and Joint International Research Laboratory for Precision Chemistry and Molecular Engineering, Feringa Nobel Prize Scientist Joint Research Centre, School of Chemistry and Molecular Engineering, East China University of Science and Technology, Shanghai 200237,* [2]*Materials Innovation Factory and Department of Chemistry, University of Liverpool, Liverpool L69 7ZD,* [3]*Department of Chemistry, The Hong Kong University of Science and Technology, Clear Water Bay, Kowloon 999077,* [4]*Leverhulme Research Centre for Functional Materials Design, University of Liverpool, Liverpool L69 7ZD*

**Corresponding authors: zhangweiwei@ecust.edu.cn; c.boott@liverpool.ac.uk; jlhua@ecust.edu.cn; aicooper@liverpool.ac.uk;* [†]X. Liu, H. Qu, and C. Li contributed equally to this work.

Cite this: *CCS Chem*. **2026**, Just Published. DOI: 10.31635/ccschem.026.202607343

Most organic materials investigated for photocatalytic hydrogen production are extended solids, such as carbon nitride, covalent organic frameworks, or conjugated organic polymers. Conjugated molecules with well-defined architectures provide an alternative platform that enables mechanistic investigations at the molecular level. Here, we present the synthesis of chemically stable conjugated macrocycles via aromatic imine condensation, followed by oxidative cyclization. These macrocycles exhibited efficient light absorption, good water affinity, and effective photoinduced charge separation. Combined transient absorption spectroscopy and density functional theory (DFT) analyses revealed that the heterocycle-based triangular macrocycle (TMC) adopted a distinctive C_2-symmetric conformation that directed charge carriers toward spatially separated edges of the framework, leading to pronounced charge delocalization and prolonged excited-state lifetimes. In aqueous dispersions, the imidazole-based macrocycle (TMC-N) further formed photoinduced polarons, facilitating charge separation and transport. As a result, protonated TMC-N achieved a sacrificial hydrogen evolution rate (HER) of 1390 $\mu mol \cdot g^{-1} \cdot h^{-1}$ under AM 1.5G irradiation (100 $mW \cdot cm^{-2}$). This well-defined platform enabled a multiscale photophysical investigation bridging theoretical models, discrete molecular species, and their supramolecular aggregates under photocatalytic conditions, revealing a structure–symmetry–excited-state dynamics relationship in supramolecular macrocycles and offering a molecular design strategy for organic photocatalysts.

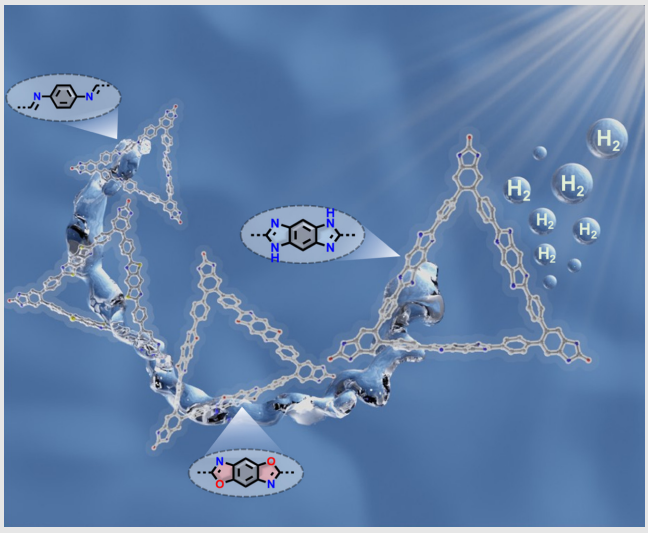

Keywords: **macrocycles, heterocycle, photocatalysis, hydrogen production, structure-activity relationships**

Citation: *CCS Chem*. **2026**, Just Published. DOI: 10.31635/ccschem.026.202607343
Link to VoR: https://doi.org/10.31635/ccschem.026.202607343

Introduction

Purely organic materials featuring well-defined 3-dimensional structures, such as discrete cages and macrocycles, covalent organic frameworks (COFs), and hydrogen-bonded organic frameworks have received interest in applications such as adsorption and separation,[1-3] energy storage[4] and other areas.[5,6] Incorporating π-conjugated organic chromophores into these materials offers chemical tunability, light-harvesting, and charge transfer, creating avenues for their development in photocatalytic water splitting.[7-11] Current research efforts into these organic systems predominantly focus on chemical structures[12] and active sites.[10] Nevertheless, the fundamental correlation between their architectures and the resulting excited-state dynamics[13] remains poorly understood. Particularly, understanding the interplay between structural symmetry and the spatial distribution of electron-hole pairs upon photoexcitation is crucial for designing organic photocatalysts with enhanced water splitting performance, ultimately with the goal of promoting overall water splitting using visible light.

In this respect, molecular macrocycles and cages represent a novel class of porous materials featuring discrete shape-persistent structures.[14,15] They can be thought of as the minimal pore units of extended COFs and metal organic frameworks (MOFs)[16-19] and are therefore adopted as model systems to facilitate systematic structure–property investigations at the molecular level.[18,20] Furthermore, their rigid scaffolds can organize photoactive units into confined geometries that may facilitate charge separation and prolong excited-state lifetimes by reducing collisional quenching.[21,22] Compared with extended framework materials, macrocycles and cages exhibit enhanced solution processability, which can simplify their structure determination, synthetic postmodification, and mechanistic studies.[23] This has spurred interest in exploring macrocycles and cages for photocatalytic water splitting under both homogeneous and heterogeneous conditions.[21,24-26] However, many macrocycles constructed through dynamic covalent chemistry (DCC) suffer from structural instability under practical photocatalytic conditions, such as acidic or aqueous environments,[27] limiting their application in photocatalytic water splitting. Although several synthetic strategies, including the Povarov reaction,[28] amidation,[29] and "tying" approaches,[30] have been developed to improve the chemical robustness of macrocycles and cages, these methods often involve multistep procedures and may complicate the efficient preparation of diverse macrocycles. Consequently, structurally defined and chemically robust conjugated macrocycles suitable for investigating excited-state processes in photocatalysis remain scarce.

Inspired by stabilization strategies developed in COF chemistry, oxidative cyclization coupled with aromatic imine condensation provides an effective route to heterocycle-containing conjugated systems.[31-34] Such transformations can convert dynamic imine linkages into chemically robust heterocyclic motifs while preserving molecular topology and enabling the structural diversification.[35] Here, we construct conjugated triangular macrocycles (TMC) and related dimeric macrocycles (DMC) featuring imidazole (-N) and oxazole (-O) bridges through imine condensation followed by oxidative cyclization, with imine counterpart (TMC-I) as a comparison. The resulting heterocyclic macrocycles exhibit enhanced stability, broad light-harvesting capability, and efficient photogenerated charge separation. Density functional theory (DFT) calculations combined with femtosecond transient absorption (TA) spectroscopy reveal that TMC-N and TMC-O adopt twisted C_2-symmetric geometries, which promote delocalized electron distribution during excited-state relaxation. Moreover, the aggregated dispersion of TMC-N in ascorbic acid solution promotes the formation of photoinduced polarons, facilitating charge separation and transport and thereby contributing to the enhanced photocatalytic activity. Consequently, protonation of the imidazole units further improves sacrificial hydrogen evolution rate (HER) to 1390 $\mu mol \cdot g^{-1} \cdot h^{-1}$ under AM 1.5 G simulated solar irradiation (100 $mW \cdot cm^{-2}$). This work establishes a platform for constructing shape-persistent conjugated macrocycles and reveals how molecular symmetry governs excited-state dynamics, providing design principles for efficient organic photocatalysts.

Experimental Methods

TMC can be regarded as an analogue of the fundamental repeating units in COFs that feature trigonal (hxl),[36] Kagome (kgm)[37] and hexagonal tungsten bronze (htb)[38] topologies (Figure 1a), which typically require the building blocks with an interior angle of approximately 60°. 4,5-Disubstituted benzimidazolone incorporates the angle of 62.9°, fulfilling the geometrical requirement for TMCs.[39] Furthermore, imidazolone subunits facilitate directional hydrogen bond formation, either among periphery entities or with water molecules,[40] thus creating hydrophilic binding sites that might improve hydrogen evolution performance in photocatalytic water splitting.

To investigate the optimal conditions for synthesizing heterocycle-linked macrocycles, model compounds containing imine bonds (M–I), imidazole (M–N), or oxazole (M–O) rings were prepared by reacting the hydrochloride (HCl) form of *p*-phenylenediamine derivatives with benzaldehyde via direct oxidative cyclization under air, catalyzed by trifluoroacetic acid (TFA) or pyridine in methanol (Figure 1c). Following the strategy established in the model reactions, a series of macrocycles was

Citation: *CCS Chem.* **2026**, Just Published. DOI: 10.31635/ccschem.026.202607343
Link to VoR: https://doi.org/10.31635/ccschem.026.202607343

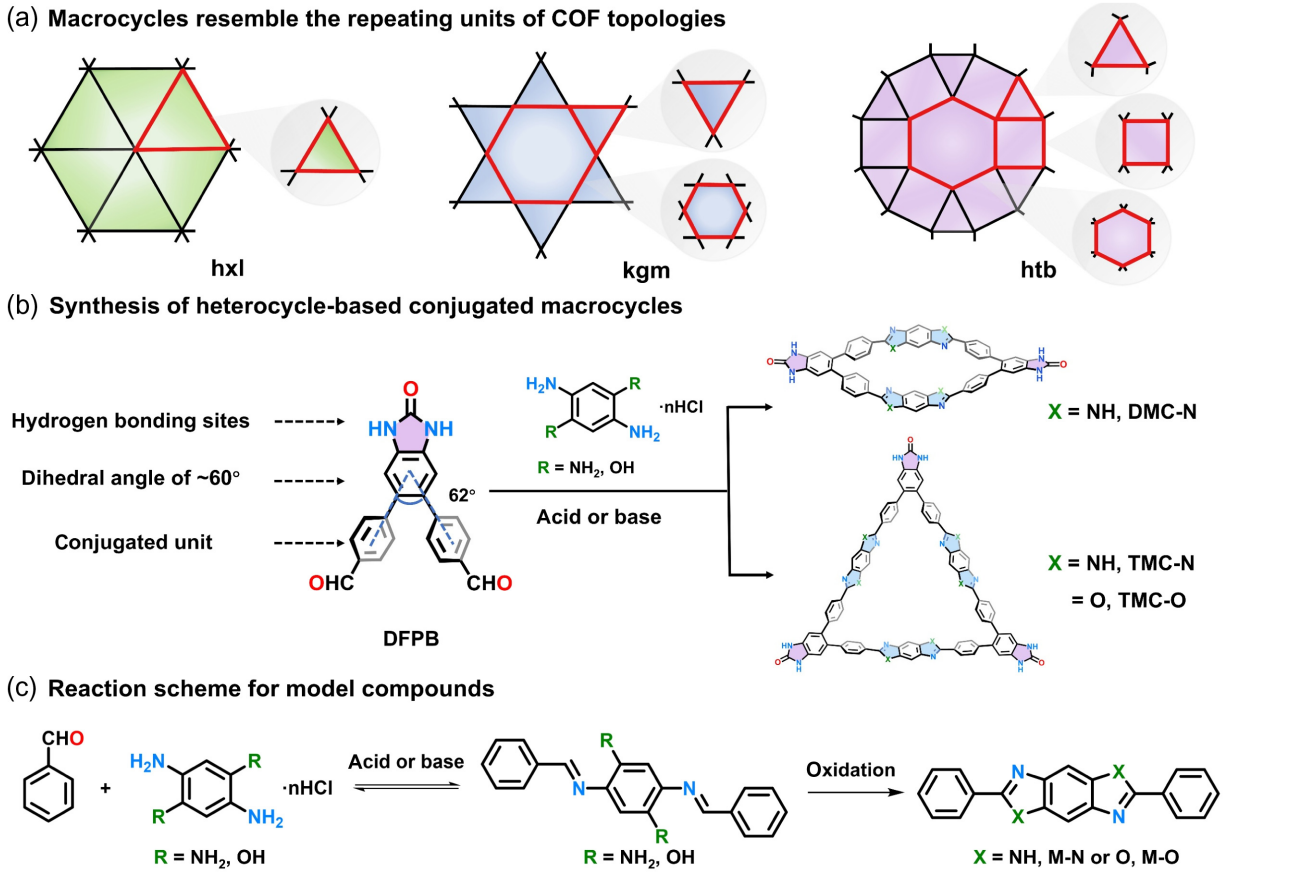

Figure 1 | *(a) Macrocycles resemble the repeating units in COF topologies. (b) Design and synthesis of N-, O-heterocycle-based dimer (DMC-N) and triangle macrocycles (TMC-N, -O). (c) Synthesis of model compounds.*

synthesized (yield >70%) by reacting the vertices, 5,6-di (4,4′-formylphenyl)-2H-benzimidazolone (DFPB), with linear linkers, specifically *p*-phenylenediamine and its derivatives, in methanol at 65 °C (Figure 1b and Supporting Information Table S1).

Catalysed by TFA, imidazole-containing TMC was formed, which precipitated directly from the reaction mixture and was further treated with ammonium hydroxide to yield the neutralized TMC-N. Using pyridine instead of TFA, the reaction selectively yielded the corresponding dimeric macrocycle DMC-N. The oxazole-containing TMC-O was prepared through the two-step reaction used for the M–O model compound.[41] The structural evolution of the intermediate imine macrocycles (DMC-NH_2 and TMC-OH) into the corresponding heterocyclic frameworks further supports the effectiveness of the oxidative cyclization strategy in enhancing macrocycle stability (Supporting Information Figures S1 and S2). For comparison, imine-linked TMC-I was synthesized under TFA catalysis to evaluate the effectiveness of the heterocycle structures on macrocycle stability and properties (Supporting Information Section 2).

All structures were comprehensively characterized (e.g., ^{1}H nuclear magnetic resonance (NMR), ^{13}C NMR, high-resolution mass spectrometry-electrospray ionization, infrared and single crystal X-ray diffraction, Supporting Information Section 4 and Figures S79–110, Tables S10–S13). The scope of this synthetic strategy was further examined using thiazole-based analogues. Matrix-assisted laser desorption ionization time-of-flight mass spectrometry analysis of the crude mixtures revealed macrocyclic species corresponding to dimer, triangle, and tetramer topologies (Supporting Information Figure S3 and Table S2). Single crystals obtained directly from the reaction mixture were isolated in quantities that allowed only X-ray diffraction analysis, confirming the formation of the thiazole-linked triangular macrocycle (TMC-S).

To further understand the structural preferences of these systems, DFT calculations were performed on the corresponding macrocycles (Supporting Information Figures S4 and S5). The calculations indicate that the triangular topology is thermodynamically favored, while the modest energy differences among the possible architectures suggest that multiple macrocyclic geometries (dimer and tetramer) can be kinetically accessible

Citation: *CCS Chem.* **2026**, Just Published. DOI: 10.31635/ccschem.026.202607343
Link to VoR: https://doi.org/10.31635/ccschem.026.202607343

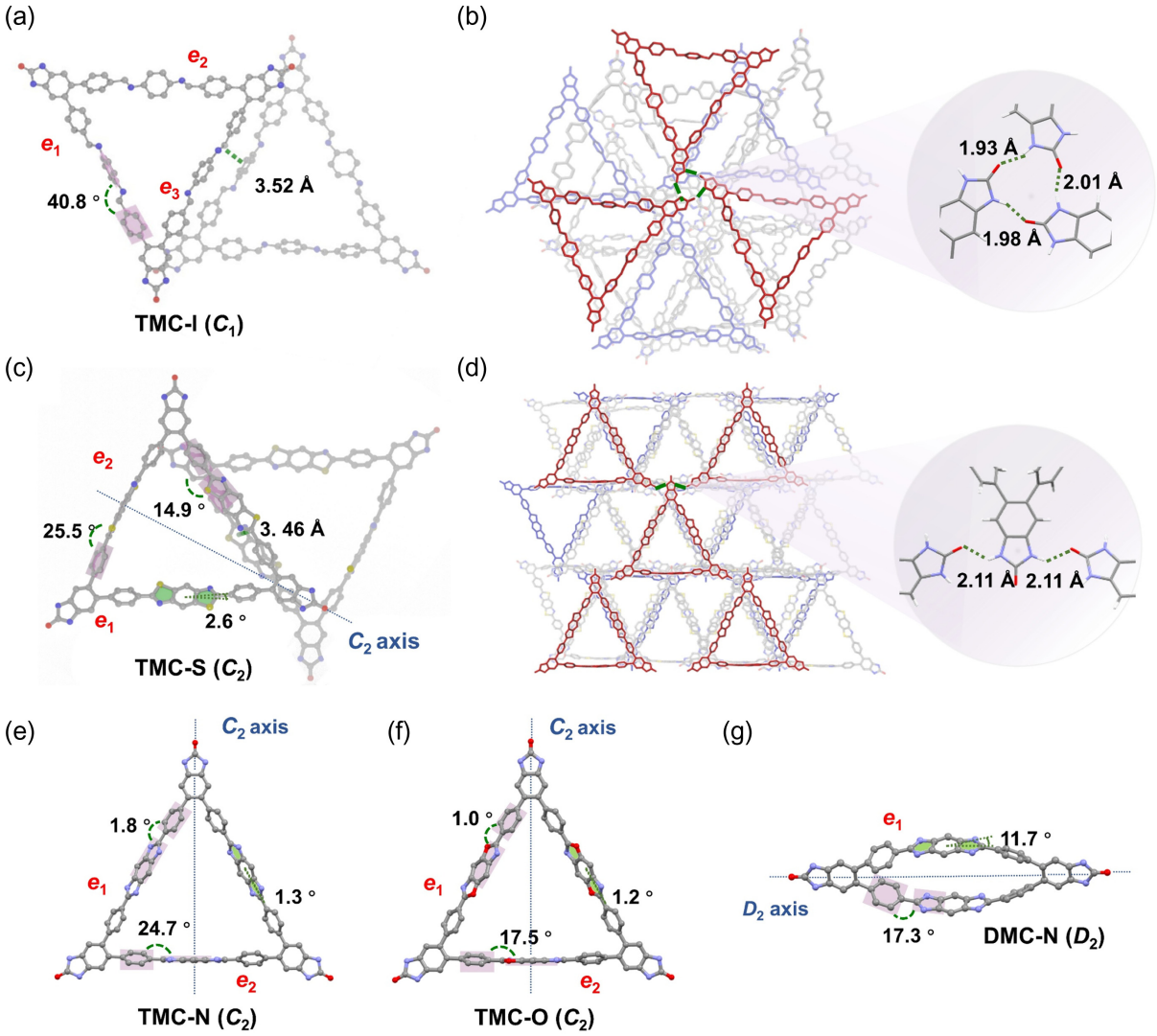

Figure 2 | *(a, b) Single-crystal and packing structures of TMC-I. (c, d) Single-crystal and packing structures of TMC-S. All structures are solvated, solvent molecules omitted for clarity. (e–g) Minimum-energy configurations of TMC-N, TMC-O, and DMC-N optimized by DFT calculations at the CAM-B3LYP/def2-SVP level. Hydrogen atoms are omitted for clarity. Atom colors: carbon, gray; nitrogen, blue; oxygen, red; and sulfur, yellow*

under certain conditions. The experimentally observed product distribution reflects the interplay between thermodynamic stability and kinetic accessibility (see details in Supporting Information Section 3.1).

Results and Discussion

Structural characterization

Hexagonal single crystals of TMC-I were obtained through slow evaporation of ethanol into a dimethyl sulfoxide (DMSO) solution. Single-crystal X-ray diffraction analysis confirmed the triangular conformation of TMC-I (Figure 2a). Due to its highly strained geometry, the phenyl rings in the macrocycle linkages exhibited a large torsion angle of approximately 40° with the adjacent phenyl groups in DFPB units, indicating the diminished conjugation of TMC-I. Besides the intrinsic cavity of TMC-I, three TMC-I molecules formed an extrinsic triangular pore via a hydrogen-bonded ternary imidazolone (Figure 2b). The two-dimensional (2D) hydrogen-bonding layer was identified, which further assembled into a three-dimensional (3D) superstructure via π–π stacking interactions with an interlayer distance of 3.52 Å.

A small amount of TMC-S crystallized directly from the crude reaction mixture as rod-shaped crystals, enabling structural analysis. In contrast to TMC-I, TMC-S features a more highly conjugated framework with a persistent C_2-symmetric conformation (Figure 2c). Two kinds of benzothiazole edges (e_1 and e_2) in TMC-S displayed different degrees of conjugation with the adjacent phenyl groups,

Citation: *CCS Chem.* **2026**, Just Published. DOI: 10.31635/ccschem.026.202607343
Link to VoR: https://doi.org/10.31635/ccschem.026.202607343

exhibiting a torsion angle of 14.9° and 25.5°, respectively. Unlike the hydrogen-bonded ternaries in TMC-I, the single-crystal structure of TMC-S exhibited linear hydrogen bonding patterns within a layer, facilitating the formation of a subsequent hierarchical 2D hydrogen-bonding network (Figure 2d). The enhanced planarity and favorable π–π stacking interactions of TMC-S, with a packing distance of 3.46 Å between benzothiazole linkages, resulted in a 3D connected channel (Supporting Information Figure S6). The single-crystal structure of TMC-S provides direct structural evidence for the formation of heterocycle-linked TMCs, validating the effectiveness of the oxidative cyclization strategy for constructing conjugated macrocycles.

The structures of TMC-N, TMC-O, and DMC-N were constructed and optimized by DFT calculations (Figure 2e–g), since attempts to grow X-ray-quality crystals were unsuccessful. The optimized DMC-N adopted a D_2-symmetric structure (Figure 2g) with two nearly parallel heterocycles (e_1). Due to the highly strained geometries, the heterocycles in DMC-N showed curved configuration with the dihedral angles of 11.7°. Additionally, the phenyl rings displayed torsion angles of 17.3°. In comparison with [2+2] geometries, the minimum-energy configurations of TMC-N and TMC-O (Figure 2e,f) exhibited lower symmetric (C_2) structures with two distinct nonequivalent edges (e_1 and e_2), which was also observed in the single-crystal structure of TMC-S. As the phenyl rings in DFPB could not favorably orient perpendicularly to the benzimidazolone units, a C_2-symmetric conformation of TMC-N and TMC-O was more thermodynamically favorable than a C_3-symmetric arrangement. The structural asymmetry of edges in TMC-N and TMC-O resulted in their different degree of planarization between heterocycles and phenyl rings. For example, in TMC-N, two imidazole rings were nearly planar with phenyl rings with a dihedral angle of ~2° in e_1, while the structural twist between imidazole rings and phenyl group was found in e_2 with a higher torsion (24.7°). Such structural asymmetry and twisting of TMC-N and TMC-O might influence the electron distribution and dynamic behaviors in both their ground and excited states.[9,42]

The amorphous, desolvated samples (TMC-I, TMC-N, TMC-O and DMC-N; morphologies in Supporting Information Figures S10–S17) were activated at 373 K under vacuum for 12 h, and thermogravimetric analysis confirms that the materials remain stable well above this temperature (Supporting Information Figure S9). Corresponding CO_2 adsorption data are provided in the Supporting Information Figures S7 and S8 (Figure 3a). Water vapor sorption measurements revealed that TMC-N exhibited a significantly higher uptake of 12.0 mmol · g^{-1} (298 K, P/P_{sat} = 0.7) (Figure 3b), exceeding those of TMC-I (5.4 mmol · g^{-1}), TMC-O (4.9 mmol · g^{-1}), and DMC-N (4.9 mmol · g^{-1}) under identical conditions. This enhanced water affinity was attributed to the abundant hydrogen-bonding sites provided by the benzimidazole linkages in TMC-N. These results indicated a higher hydrophilicity of TMC-N, beneficial for photocatalytic water splitting.

Photophysical characterization

Efficient light harvesting across the solar spectrum is essential for photocatalytic hydrogen evolution. To investigate the photophysical properties, UV–vis absorption and photoluminescence (PL) spectra were measured both in the solid state and solution (Supporting Information Figures S18–S23). All macrocycles exhibited broader visible-light absorption and red-shifted absorption maxima (~50 nm) relative to the model compounds in solution (Figure 3c and Supporting Information Figure S19), attributable to the extended conjugation of the rigid macrocycles. Among them, TMC-N displayed the highest molar extinction coefficient (ε = 1.52 × 10^5 M^{-1} · cm^{-1} at λ_{max} = 363 nm) (Supporting Information Figure S20 and Table S3), reflecting its stronger light-harvesting properties. In the solid state, diffuse reflectance spectra of TMC-N revealed extended absorption up to ~600 nm (Figure 3d), consistent with a narrowed optical bandgap of 2.23 eV determined from Tauc plot analysis (Supporting Information Figure S24).

To gain a more in-depth understanding of the driving force for proton reduction, the energy band positions of the macrocycle photocatalysts were determined. Mott–Schottky analysis was measured to evaluate the flatband potential and semiconductor type (Supporting Information Figure S25). All macrocycles featured a positive slope, disclosing their n-type semiconductor character. By combining the conduction band positions with E_g, the valence band potential (E_{VB}) of TMC-N was determined as 1.34 V. Cyclic voltammetry measurements were additionally performed to further confirm the band edge positions and investigate the electrochemical behavior of the photocatalysts (Supporting Information Figure S26 and Table S3). The experimentally determined energy-level alignments (Figure 3e) validate the thermodynamic feasibility of these macrocycles in fulfilling the criteria for sacrificial proton reduction.

The efficiency of charge separation and migration are critical factors that influence the overall performance of photocatalytic hydrogen evolution. To elucidate the mobility of photogenerated electrons, the photoelectrochemical properties of these macrocycles were investigated (Supporting Information Figures S27 and S28). At a bias voltage of −0.2 V (vs Ag/AgCl), the photocurrent density of TMC-N was found to be ~0.4 μA · cm^{-2}, surpassing that of TMC-I, -O, and DMC-N. Electrochemical impedance spectroscopy (EIS) demonstrated a reduction in charge transfer resistance (R_{ct}) for all macrocycles under irradiation, as indicated by their smaller diameters of alternating current impedance semicircles (Figure 3f).

Citation: *CCS Chem.* **2026**, Just Published. DOI: 10.31635/ccschem.026.202607343
Link to VoR: https://doi.org/10.31635/ccschem.026.202607343

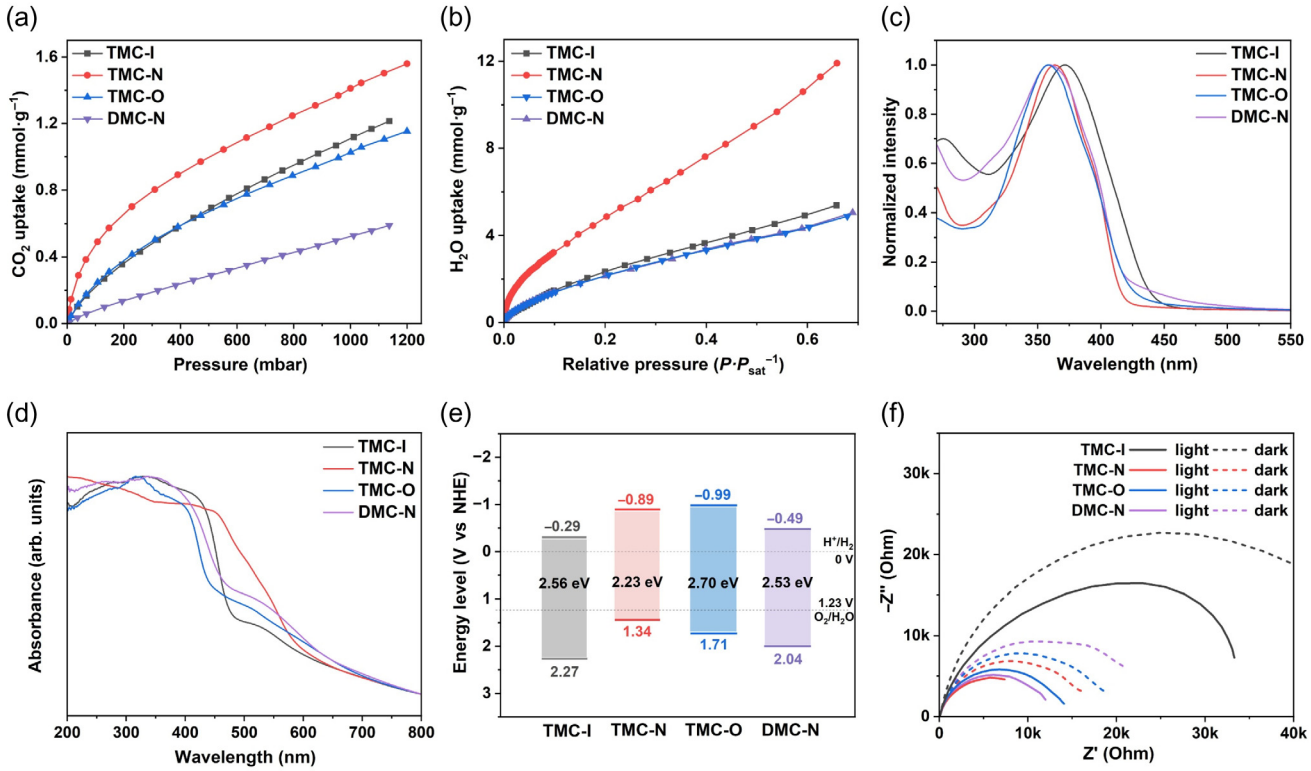

Figure 3 | *(a) CO_2 (273 K) sorption isotherms and (b) water vapor adsorption (298 K) isotherms for TMC-I, TMC-N, TMC-O, and DMC-N. (c) Normalized UV–vis spectra of macrocycles (12.5 μg · mL^{-1}) in DMSO. (d) Diffuse reflectance spectra for macrocycles in the solid state. (e) Energy-level diagrams for TMC-I, TMC-N, TMC-O, and DMC-N. (f) EIS of macrocycles, solid lines and dashed lines represent the macrocycles under light or dark conditions.*

Among these macrocycles, TMC-N exhibited the lowest R_{ct} of the macrocycles, indicating superior charge transfer dynamics, consistent with its enhanced photocurrent response.

Photocatalysis and mechanism studies

The sacrificial photocatalytic activities of these macrocycles and their corresponding model compounds for hydrogen production were evaluated on a high-throughput photocatalytic water splitting platform using ascorbic acid as a sacrificial agent under AM 1.5G illumination at ambient pressure (reaction setup in Supporting Information Figures S29 and S30). Initial investigations on the HERs of the model compounds (Supporting Information Figure S31) revealed that no hydrogen had evolved in the absence of a platinum cocatalyst.

Compared with linear model compounds, the macrocycles demonstrated notably increased photocatalytic performance. This enhancement was attributed to the broader absorption range, enabling more efficient photon harvesting under irradiation. Specifically, upon loading Pt into the macrocycles, the average HERs of TMC-N and TMC-O could be further enhanced, reaching 697 and 147 μmol · g^{-1} · h^{-1}, respectively. TMC-I and DMC-N evolved hydrogen only with 3% Pt loading (HERs: 18 and 239 μmol · g^{-1} · h^{-1}, respectively). However, TMC-N exhibited hydrogen evolution only under acidic conditions, with no activity observed in neutral or alkaline conditions (Supporting Information Figure S32). Furthermore, ^{1}H NMR analysis of the photocatalysts postreaction, indicated that the heterocycle-based macrocycles underwent no discernible changes, thus demonstrating robust structural stability at least under these sacrificial photocatalytic conditions (Supporting Information Figures S33–S36).

To probe the excited states and charge-transfer dynamics of these macrocycles, time-dependent (TD)-DFT calculations (Supporting Information Figures S37–S41 and Table S4) combined with time-correlated single-photon counting (TCSPC; Supporting Information Figures S42–S43 and Tables S5–S6) and femtosecond TA UV/Vis spectroscopy (Figure 4, Supporting Information Figures S44–S51, and Table S7) were employed.

In solution, TA spectra of TMC-N, TMC-O, and DMC-N displayed a broad photoinduced absorption (PIA) band (450–700 nm), assigned to S_1-state absorption (Supporting Information Figures S44 and S45). A weaker feature at 420–430 nm overlapped with negative signals below 500 nm, attributed to ground-state bleaching (GSB) and stimulated emission (SE), consistent with

Citation: *CCS Chem.* **2026**, Just Published. DOI: 10.31635/ccschem.026.202607343
Link to VoR: https://doi.org/10.31635/ccschem.026.202607343

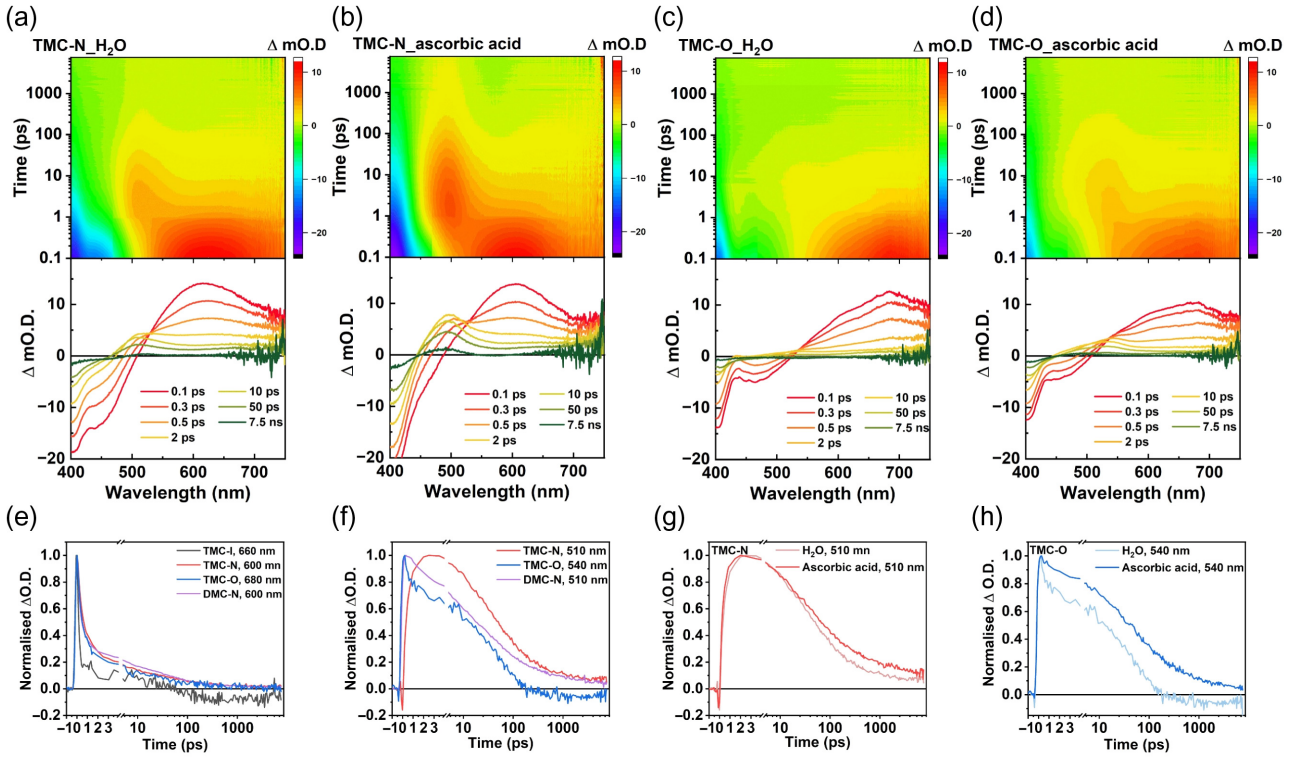

Figure 4 | *The complete TA surface of TMC-N and TMC-O aggregates (a, c) in water (0.1 mg · mL^{-1}) and (b, d) in the presence of ascorbic acid (0.1 M), and the corresponding TA spectra at selected pump-probe time delays following 390 nm excitation with a power of 700 μW; ΔO.D. = difference in optical density. (e, f) The normalized kinetic traces showing the decay of the PIA of TMC-N, DMC-N, TMC-I, and TMC-O at selected wavelengths. (g, h) The comparison of normalized kinetics of TMC-N and TMC-O probed at 510 and 540 nm, with and without ascorbic acid, respectively.*

steady-state absorption and PL spectra (Figure 3d and Supporting Information Figure S22). Compared with model compounds, the redshift PIA bands indicated the formation of delocalized excitons in TMC-N, DMC-N, and TMC-O, whereas TMC-I showed localized excitonic behavior similar to its model compounds M–I.

The spectroscopic observations of heterocyclic TMCs compared with TMC-I suggested that the spatial distribution of the excited states was closely related to their distinct conformation (Figure 2). TD-DFT calculations revealed that the S_1 natural transition orbitals (NTOs) of TMC-N, TMC-O, and DMC-N were predominantly delocalized along the two symmetric edges (e_1, Supporting Information Figures S37–S40), indicating that the heterocycle-based linkages served as the principal channels for electron transport (details in Supporting Information Section 3.9). In contrast, the S_1 states of TMC-I were largely confined to a single edge, attributed to the twisted conformation of each of the edges. Such localization implied weaker electronic coupling between repeating units, thereby limiting excitonic coherence and long-range charge transport, consistent with the markedly shorter excited-state lifetime of TMC-I (Supporting Information Figure S47 and Table S7).

We next examined the aggregation-dependent photophysical behavior of the macrocycles in water and under photocatalytic conditions, that is, in the presence of ascorbic acid (Figure 4a–d and Supporting Information Figures S48–S49). At early delay times (0.1 ps), the TA spectra were dominated by singlet excitonic features, showing a broad excited-state absorption (ESA) band (>450 nm) with overlapping GSB and SE signals. These signatures decayed rapidly in TMC-N, TMC-O, and DMC-N, with half-lifetimes of ~0.5 ps, while TMC-I exhibited a slightly faster decay (Figure 4e). Within ~50 ps, new long-lived absorption bands emerged at ~510 nm for TMC-N and DMC-N and ~540 nm (weaker) for TMC-O (Figure 4f), which were further enhanced in ascorbic acid and dominated beyond 50 ps (Figure 4b,d,g,h). In contrast, no analogous signal was observed for TMC-I (Supporting Information Figure S48), indicating inefficient charge separation, likely due to its low planarity and weak interlayer π–π interactions. Among them, TMC-N exhibited the most persistent polaron signal, indicative of more effective stabilization of photogenerated electrons, whereas DMC-N showed faster decay, consistent with their respective photocatalytic activities. These long-lived signals were assigned to electron polarons

Citation: *CCS Chem.* **2026**, Just Published. DOI: 10.31635/ccschem.026.202607343
Link to VoR: https://doi.org/10.31635/ccschem.026.202607343

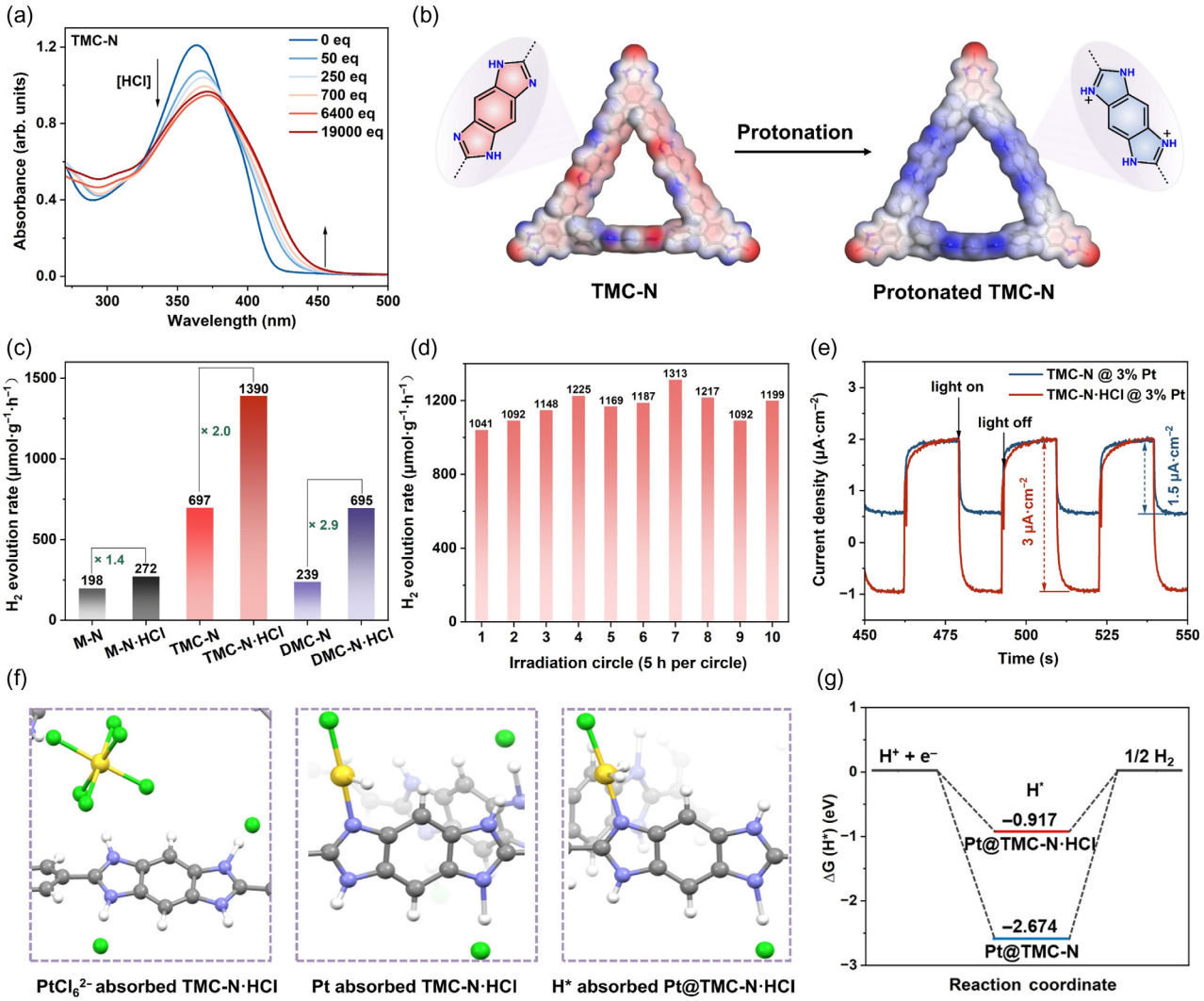

Figure 5 | *(a) Electrostatic potential surface of TMC-N and protonated TMC-N. (b) HCl titration absorption spectra of TMC-N (12.5 μg · mL^{-1} in DMSO) (c) HERs for materials and their protonated derivatives loaded 3% Pt. Test condition: 1 mg material in 0.1 M ascorbic acid solution, 0.8 μL H_2PtCl_6 (8 wt % aqueous solution), AM 1.5 G illumination for 5 h. (d) Longer-term hydrogen evolution experiments for TMC-N · HCl loaded 3% Pt, the photocatalysts and ascorbic acid solution remained unchanged during the test. (e) Photocurrent density-time plots of TMC-N · HCl and TMC-N · HCl loaded 3% Pt measured at −0.2 V vs Ag/AgCl. (f) The geometric structures of TMC-N · HCl with $PtCl_6^{2-}$, Pt atom, and H* absorbed. Atom colors: carbon, gray; nitrogen, blue; platinum, yellow; chloride, green; hydrogen, white. (g) Calculated free energy diagram for photocatalytic hydrogen evolution. The DFT calculations were performed at the CAM-B3LYP/def2-SVP level.*

based on their quenching under oxygenated conditions (Supporting Information Figure S50). Similar polaronic signatures have been widely reported in conjugated polymer photocatalysts,[43,44] supramolecular nanoaggregate systems,[45,46] and inorganic photocatalysts.[47,48]

Furthermore, protonation of imidazole linkages in ascorbic acid solution likely increased the electron-accepting character of TMC-N and modulated intermolecular interactions. The long-lived electron polaron signals were observed only in the aggregated state, indicating that charge separation and stabilization likely occurred across π-stacked architectures, giving rise to intermolecular delocalized polarons. Such delocalization enhanced charge mobility within and between aggregates, facilitating efficient electron transfer to deposited Pt nanoparticles.[46] TCSPC measurements further revealed that incorporation of Pt prolongs the fluorescence lifetime of TMC-N from 0.62 to 1.08 ns (Supporting Information Figure S43 and Table S6), reflecting the interfacial electronic coupling for electron extraction and suppression of nonproductive recombination pathways. Collectively, these findings revealed that the enhanced photocatalytic

Citation: *CCS Chem.* **2026**, Just Published. DOI: 10.31635/ccschem.026.202607343
Link to VoR: https://doi.org/10.31635/ccschem.026.202607343

performance of TMC-N arose from symmetry-enabled charge delocalization and aggregation-induced long-lived electron polarons, which facilitated efficient charge separation, transport, and interfacial electron transfer for hydrogen evolution.

Effect of protonation

Motivated by the TA results, we proposed that beyond differences in light absorption and charge-transfer kinetics, the higher performance of TMC-N relative to the other macrocycles might have arisen from protonation of the benzimidazole linkages in ascorbic acid solution. The solubility and processability of these macrocycles allowed diverse postsynthetic modifications, which could further improve their photocatalytic performance.

To probe the different optical behaviors of the macrocycles upon protonation, UV–vis and fluorescence titration experiments were performed using HCl. In the UV–vis spectra, the addition of HCl into the DMSO solutions of TMC-N and DMC-N (Figure 5a and Supporting Information Figure S52) caused a pronounced redshift (8 nm) of maximum adsorption peaks and absorption onset (>40 nm). In addition, the fluorescence of TMC-N and DMC-N was markedly quenched by HCl addition (Supporting Information Figure S53). The adsorption and fluorescence emission peaks upon HCl addition for TMC-O remained nearly unchanged (Supporting Information Figure S54, details in Supporting Information Section 3.10.1). By contrast, progressive addition of HCl into the DMSO solutions of TMC-I resulted in the disappearance of adsorption peaks at 350 or 380 nm, indicating the hydrolysis of imine bonds (Supporting Information Figure S55). Collectively, these UV–vis and fluorescence results underscored the sensitivity of imidazole-based macrocycles to protonation and their good chemical stabilities in the acidic environment.

These characteristics of imidazole-based macrocycles upon protonation allowed us to explore their photocatalytic performance. The addition of HCl into the M–N, DMC-N, and TMC-N solution in DMSO afforded the direct precipitation of protonated M–N · HCl, DMC-N · HCl, and TMC-N · HCl. The crystal structure of M–N · HCl confirmed the fully protonated imidazole rings with two chloride anions coordinated to their N–H$^+$ groups. Despite unsuccessful attempts at crystallizing DMC-N · HCl and TMC-N · HCl, ^{1}H NMR, Fourier transform infrared (FT-IR) spectra, and energy-dispersive spectroscopy (EDS) analysis verified the protonation and the presence of chloride anions (Supporting Information Figures S56–S61). Additionally, electrostatic potential (ESP) maps highlighted the electron-deficient character of the protonated imidazole groups in TMC-N, DMC-N, and M–N (Figure 5b and Supporting Information Figures S62–S63), underscoring the significant redistribution of electron density upon protonation.

All the protonated photocatalysts showed higher HERs than their nonprotonated counterparts (Figure 5c). Specifically, upon protonation, the HER of TMC-N · HCl with 3% Pt (optimization details shown in Supporting Information Figure S64) was significantly increased to 1390 μmol · g^{-1} · h^{-1}, which was two times higher than that of TMC-N. Furthermore, TMC-N · HCl exhibited a continuous increase in hydrogen evolution over time (Supporting Information Figure S65) and demonstrated excellent stability, sustaining hydrogen production for over 50 h without any obvious decline (Figure 5d). The HER performance of TMC-N · HCl under a Xe lamp (λ > 420 nm, 283 mW · cm^{-2}) was measured to be 2137 μmol · g^{-1} · h^{-1}, consistent with the expected enhancement under stronger illumination (Supporting Information Figure S66a), and compared favorably with many reported organic photocatalysts (Supporting Information Table S8). After 5 h of illumination, both the mass loss and decrease in activity were negligible (Supporting Information Figure S66b). Apparent quantum yield (AQY) measurements revealed a clear correlation between light absorption and hydrogen evolution, with the AQY reaching 0.17% at 405 nm (Supporting Information Figure S67).

The influence of anion diversity on the hydrogen evolution performance of TMC-N was also investigated by substituting HCl with formic acid (HCOOH) or TFA to protonate imidazole groups. The resulting protonated macrocycles, TMC-N · HCOOH and TMC-N · TFA, demonstrated HERs comparable with that of TMC-N · HCl, both outperforming the unprotonated TMC-N (Supporting Information Figure S68). These results highlighted that protonation of the macrocycle, rather than the specific anion, played a crucial role in enhancing photocatalytic activity.

Further investigations into how protonation affected the water affinity (Supporting Information Figure S69), optical properties (Supporting Information Figure S70), and excited-state lifetime (Supporting Information Figure S71) implied that these properties were not decisive factors behind the enhanced performance of protonated TMC-N · HCl (Supporting Information Section 3.10.2). The loading of Pt nanoparticles into TMC-N · HCl also significantly boosted the photocurrent density to ~3.0 μA · cm^{-2}, a five-fold increase over TMC-N · HCl without Pt loading (~0.5 μA · cm^{-2}) and a two-fold increase compared with Pt-loaded TMC-N (~1.5 μA · cm^{-2}), as illustrated in Figure 5e and Supporting Information Figure S72. Protonation significantly influenced the morphologies of macrocycles (Supporting Information Figures S73 and S74) suspended in water or ascorbic acid aqueous solution (0.1 M). In water, the size distribution of TMC-N · HCl particles was centered at ~1.9 μm, smaller than that of TMC-N (2.7 μm). In contrast, in ascorbic acid solution, TMC-N · HCl formed larger particles (4.4 μm) with a low polydispersity index (PDI = 0.026), as shown in Supporting Information Table S9. This substantial swelling could

Citation: *CCS Chem.* **2026**, Just Published. DOI: 10.31635/ccschem.026.202607343
Link to VoR: https://doi.org/10.31635/ccschem.026.202607343

be attributed to stronger hydrogen bonds and electrostatic interactions with ascorbic acid, leading to enhanced adsorption of TMC-N · HCl. Moreover, such swelling also facilitated the anion exchange between chloride and $PtCl_6^{2-}$ anions, as confirmed by the calculated binding energies: –3.00 eV for $PtCl_6^{2-}$ with TMC-N · HCl versus –1.96 eV with TMC-N (Supporting Information Figure S75).

In addition, X-ray photoelectron spectroscopy (XPS) and transmission electron microscopy (TEM) images of TMC-N · HCl collected after photocatalytic reactions revealed the reduction of $PtCl_6^{2-}$ to Pt^{2+}/Pt^0 and a uniform distribution of Pt nanoparticles across the surface of the macrocycle, with an average diameter of 1.5 nm (Supporting Information Figure S76 and S77). Computational models of this process are given in Figure 5f and Supporting Information Figure S78. Typically, the photocatalytic hydrogen evolution pathway was modelled by a three-state process comprising the initial state ($H^+ + e^-$), an intermediate adsorbed state (H*), and the final state (H_2).[49] The Gibbs free energy change (ΔG_{H^*}) of the intermediate state is a key descriptor for the reaction rate, with an optimal value near zero ($|\Delta G_{H^*}{}^{Pt}| \approx 0.09$ eV) for an efficient Pt cocatalyst. In this work, ΔG_{H^*} values of Pt @ TMC-N and Pt @ TMC-N · HCl were calculated to be –2.67 and –0.92 eV, ensuring both effective H* formation and rapid hydrogen desorption on Pt @ TMC-N (Figure 5g). These findings underscored that TMC-N · HCl, with protonated imidazole, served as an effective Pt binding site, crucial for optimizing hydrogen binding and release.

Conclusion

We report the synthesis of heterocycle-based conjugated macrocycles using aromatic imine condensation followed by subsequent oxidative cyclization. This integration of heterocyclic units provided these macrocycles with good chemical stability and diverse functionalities, including enhanced π-conjugation, hydrophilicity, and protonation ability. TA spectroscopy combined with theoretical calculations revealed that molecular symmetry played a key role in regulating excited-state dynamics: the C_2-symmetric triangular framework promoted electron delocalization and facilitated the formation of long-lived electron polarons in the aggregated state. These stabilized charge carriers effectively prolong excited-state lifetimes and contributed to efficient photocatalytic hydrogen evolution. Furthermore, protonation of the imidazole macrocycles TMC-N significantly enhanced the photocatalytic activity from 697 to 1390 $\mu mol \cdot g^{-1} \cdot h^{-1}$, highlighting the importance of both molecular structure and electronic environment in tuning photocatalytic performance.

Organic macrocycles and cages, which confined the photoactive units within a well-defined molecular scaffold, were sufficient to furnish a minimal yet essential platform for charge separation and transport, resembling the repeating units of extended framework materials in photocatalytic reactions. The discrete organic macrocycles and cages also provided direct mechanistic insights into the structure-property correlation and solution processability for their post-functionalization and fabrication. Our design principles emphasize the great potential of stabilization strategies developed for COF chemistry for constructing advanced conjugated macrocycles and cages in photocatalytic applications. Notably, these materials are amorphous, despite the benzimidazalone hydrogen-bonding groups. The development of analogous materials that retain crystallinity and porosity in the solid state might further improve photocatalytic properties by enhancing charge transport.[8]

Supporting Information

Supporting Information is available and includes experiment details, supplementary characterization, and analysis.

Conflict of Interest

There is no conflict of interest to report.

Funding Information

This work was supported financially by the following institutions: the National Natural Science Foundation of China (grant nos. 22271093 and 21971064), Science and Technology Commission of Shanghai Municipality, China (grant nos. 24DX1400200 and 24160711900), Programme of Introducing Talents of Discipline to Universities, China (grant no. B16017), the Fundamental and Interdisciplinary Disciplines Breakthrough Plan of the Ministry of Education of China (grant no. JYB2025XDXM404) and the Fundamental Research Funds for the Central Universities, China. X.L. acknowledges the China Scholarship Council for financial support. A.I.C. thanks the Royal Society for a Research Professorship, UK (RSRP\S2\232003). The authors also received funding from the Engineering and Physical Sciences Research Council (EP/V026887/1) and from the Leverhulme Trust via the Leverhulme Research Centre for Functional Materials Design, United Kingdom.

Acknowledgments

The authors thank the Research Centre of Analysis and Test at East China University of Science and Technology for the help with the characterization. They also wish to acknowledge Krzysztof Pawlak, Yifei Zhu, Chengxi Zhao, Hong Wang, and Jing Yang for helpful discussions.

Citation: *CCS Chem.* **2026**, Just Published. DOI: 10.31635/ccschem.026.202607343
Link to VoR: https://doi.org/10.31635/ccschem.026.202607343

References

1. Zhou, Z.; Ma, T.; Zhang, H.; Chheda, S.; Li, H.; Wang, K.; Ehrling, S.; Giovine, R.; Li, C.; Alawadhi, A. H.; Abduljawad, M. M.; Alawad, M. O.; Gagliardi, L.; Sauer, J.; Yaghi, O. M. Carbon Dioxide Capture from Open Air Using Covalent Organic Frameworks. *Nature* **2024**, *635*, 96–101.
2. Liu, M.; Zhang, L.; Little, M. A.; Kapil, V.; Ceriotti, M.; Yang, S.; Ding, L.; Holden, D. L.; Balderas-Xicohténcatl, R.; He, D.; Clowes, R.; Chong, S. Y.; Schütz, G.; Chen, L.; Hirscher, M.; Cooper, A. I. Barely Porous Organic Cages for Hydrogen Isotope Separation. *Science* **2019**, *366*, 613–620.
3. Li, L.; Zhang, X.; Lian, X.; Zhang, L.; Zhang, Z.; Liu, X.; He, T.; Li, B.; Chen, B.; Bu, X.-H. Flue Gas Desulfurization and SO_2 Recovery Within a Flexible Hydrogen-Bonded Organic Framework. *Nat. Chem.* **2025**, *17*, 727–733.
4. Zhang, R.; Daglar, H.; Tang, C.; Li, P.; Feng, L.; Han, H.; Wu, G.; Limketkai, B. N.; Wu, Y.; Yang, S.; Chen, A. X.-Y.; Stern, C. L.; Malliakas, C. D.; Snurr, R. Q.; Stoddart, J. F. Balancing Volumetric and Gravimetric Capacity for Hydrogen in Supramolecular Crystals. *Nat. Chem.* **2024**, *16*, 1982–1988.
5. Ishii, W.; Fuki, M.; Bu Ali, E. M.; Sato, S.; Parmar, B.; Yamauchi, A.; Mulyadi, C. H.; Uji, M.; Medina Rivero, S.; Watanabe, G.; Clark, J.; Kobori, Y.; Yanai, N. Macrocyclic Parallel Dimer Showing Quantum Coherence of Quintet Multiexcitons at Room Temperature. *J. Am. Chem. Soc.* **2024**, *146*, 25527–25535.
6. Ubasart, E.; Borodin, O.; Fuertes-Espinosa, C.; Xu, Y.; García-Simón, C.; Gómez, L.; Juanhuix, J.; Gándara, F.; Imaz, I.; Maspoch, D.; Von Delius, M.; Ribas, X. A Three-Shell Supramolecular Complex Enables the Symmetry-Mismatched Chemo- and Regioselective Bis-Functionalization of C_{60}. *Nat. Chem.* **2021**, *13*, 420–427.
7. Banerjee, T.; Gottschling, K.; Savasci, G.; Ochsenfeld, C.; Lotsch, B. V. H_2 Evolution with Covalent Organic Framework Photocatalysts. *ACS Energy Lett.* **2018**, *3*, 400–409.
8. Zhang, W.; Chen, L.; Dai, S.; Zhao, C.; Ma, C.; Wei, L.; Zhu, M.; Chong, S. Y.; Yang, H.; Liu, L.; Bai, Y.; Yu, M.; Xu, Y.; Zhu, X.-W.; Zhu, Q.; An, S.; Sprick, R. S.; Little, M. A.; Wu, X.; Jiang, S.; Wu, Y.; Zhang, Y.-B.; Tian, H.; Zhu, W.-H.; Cooper, A. I. Reconstructed Covalent Organic Frameworks. *Nature* **2022**, *604*, 72–79.
9. Sun, K.; Huang, Y.; Sun, F.; Wang, Q.; Zhou, Y.; Wang, J.; Zhang, Q.; Zheng, X.; Fan, F.; Luo, Y.; Jiang, J.; Jiang, H.-L. Dynamic Structural Twist in Metal–Organic Frameworks Enhances Solar Overall Water Splitting. *Nat. Chem.* **2024**, *16*, 1638–1646.
10. Zhou, Q.; Guo, Y.; Zhu, Y. Photocatalytic Sacrificial H_2 Evolution Dominated by Micropore-Confined Exciton Transfer in Hydrogen-Bonded Organic Frameworks. *Nat. Catal.* **2023**, *6*, 574–584.
11. Zhang, G.; Lan, Z.; Wang, X. Conjugated Polymers: Catalysts for Photocatalytic Hydrogen Evolution. *Angew. Chem. Int. Ed.* **2016**, *55*, 15712–15727.
12. Zhang, W.; Yu, M.; Liu, T.; Cong M.; Liu, X.; Yang, H.; Bai, Y.; Zhu, Q.; Zhang, S.; Gu, H.; Wu, X.; Zhang, Z.; Wu, Y.; Tian, H.; Li, X.; Zhu, W.-H.; Cooper, A. I. Accelerated Discovery of Molecular Nanojunction Photocatalysts for Hydrogen Evolution by Using Automated Screening and Flow Synthesis. *Nat. Synth.* **2024**, *3*, 595–605.
13. Cai, B.; Brnovic, A.; Pavliuk, M.; Hammarström, L.; Kloo, L.; Barnett, S.; Tian, H. Organic Crystalline Nanoparticles with a Long-Lived Charge-Separated State for Efficient Photocatalytic Hydrogen Production. *Nat. Chem.* **2026**, *18*, 723–730.
14. Jin, Y.; Yu, C.; Denman, R. J.; Zhang, W. Recent Advances in Dynamic Covalent Chemistry. *Chem. Soc. Rev.* **2013**, *42*, 6634.
15. Zarra, S.; Wood, D. M.; Roberts, D. A.; Nitschke, J. R. Molecular Containers in Complex Chemical Systems. *Chem. Soc. Rev.* **2015**, *44*, 419–432.
16. Cooper, A. I. Porous Molecular Solids and Liquids. *ACS Cent. Sci.* **2017**, *3*, 544–553.
17. Hosono, N.; Kitagawa, S. Modular Design of Porous Soft Materials via Self-Organization of Metal–Organic Cages. *Acc. Chem. Res.* **2018**, *51*, 2437–2446.
18. Wang, K.; Zhong, Y.; Dong, W.; Xiao, Y.; Ren, S.; Li, L. Intermediate Formation of Macrocycles for Efficient Crystallization of 2D Covalent Organic Frameworks with Enhanced Photocatalytic Hydrogen Evolution. *Angew. Chem. Int. Ed.* **2023**, *62*, e202304611.
19. Sánchez-Naya, R.; Cavalieri, J. P.; Albalad, J.; Cortés-Martínez A.; Wang, K.; Fuentes-Espinosa, C.; Parella, T.; Fiori S.; Ribas E.; Mugarza A.; Ribas X.; Faraudo J.; Yaghi O. M.; Imaz I.; Maspoch D. Excision of Organic Macrocycles from Covalent Organic Frameworks. *Science* **2025**, *388*, 1318–1323.
20. Chen, Y.; Liu, R.; Guo, Y.; Wu, G.; Sum, T. C.; Yang, S.; Jiang, D. Hierarchical Assembly of Donor–Acceptor Covalent Organic Frameworks for Photosynthesis of Hydrogen Peroxide from Water and Air. *Nat. Synth.* **2024**, *3*, 998–1010.
21. Yang, J.; Shi, R.; Mao, L.-L.; Xiao, H.; Zeng, Y.; Liao, G.; Weng, Y.; Li, X.-B.; Zhao, J.; Zhao, Y.; Zhang, T.; Tung, C.-H.; Wu, L.-Z.; Cong, H. Photo-Induced Intramolecular Charge Transfer in Strained Organic Cage Containing Orthogonally Arranged Donors and Acceptors. *CCS Chem.* **2024**, *6*, 1920–1928.
22. Xu, Y.; Wang, B.; Kaur, R.; Minameyer, M. B.; Bothe, M.; Drewello, T.; Guldi, D. M.; von Delius, M. A Supramolecular [10]CPP Junction Enables Efficient Electron Transfer in Modular Porphyrin–[10]CPP⊃Fullerene Complexes. *Angew. Chem. Int. Ed.* **2018**, *57*, 11549–11553.
23. Le, P. H.; Liu, A.; Zasada, L. B.; Geary, J.; Kamin, A. A.; Rollins, D. S.; Nguyen, H. A.; Hill, A. M.; Liu, Y.; Xiao, D. Nitrogen-Rich Conjugated Macrocycles: Synthesis, Conductivity, and Application in Electrochemical CO_2 Capture. *Angew. Chem. Int. Ed.* **2024**, *64*, e202421822.
24. Mei, J.-H.; Lai, S.; Gong, Y.-N.; Shi, W.-J.; Deng, J.-H.; Lu, T.-B.; Zhong, D.-C. A Supramolecular-Nanocage-Based Framework Stabilized by π–π Stacking Interactions with Enhanced Photocatalysis. *Angew. Chem. Int. Ed.* **2024**, *64*, e202413413.
25. Li, N.; Li, Y.; Wang, Z.; Cao, T.; Liu, C.; Wang, H.; Li, G.; He, G. Directional Electron Flow in a Selenoviologen-Based

Citation: *CCS Chem.* **2026**, Just Published. DOI: 10.31635/ccschem.026.202607343
Link to VoR: https://doi.org/10.31635/ccschem.026.202607343

Tetracationic Cyclophane for Enhanced Visible-Light-Driven Hydrogen Evolution. *Angew. Chem. Int. Ed.* **2024**, *63*, e202410525.
26. Wu, K.; Li, K.; Chen, S.; Hou, Y.; Lu, Y.; Wang, J.; Wei, M.; Pan, M.; Su, C. The Redox Coupling Effect in a Photocatalytic Ru^{II} -Pd^{II} Cage with TTF Guest as Electron Relay Mediator for Visible-Light Hydrogen-Evolving Promotion. *Angew. Chem. Int. Ed.* **2020**, *59*, 2639–2643.
27. Belowich, M. E.; Stoddart, J. F. Dynamic Imine Chemistry. *Chem. Soc. Rev.* **2012**, *41*, 2003–2024.
28. Alexandre, P.; Zhang, W.; Rominger, F.; Elbert, S. M.; Schröder, R. R.; Mastalerz, M. A Robust Porous Quinoline Cage: Transformation of a [4+6] Salicylimine Cage by Povarov Cyclization. *Angew. Chem. Int. Ed.* **2020**, *59*, 19675–19679.
29. Bhat, A. S.; Elbert, S. M.; Zhang, W.; Rominger, F.; Dieckmann, M.; Schröder, R. R.; Mastalerz, M. Transformation of a [4+6] Salicylbisimine Cage to Chemically Robust Amide Cages. *Angew. Chem. Int. Ed.* **2019**, *13*, 8911–8915.
30. Liu, M.; Little, M. A.; Jelfs, K. E.; Jones, J. T. A.; Schmidtmann, M.; Chong, S. Y.; Hasell, T.; Cooper, A. I. Acid- and Base-Stable Porous Organic Cages: Shape Persistence and pH Stability via Post-Synthetic "Tying" of a Flexible Amine Cage. *J. Am. Chem. Soc.* **2014**, *136*, 7583–7586.
31. Waller, P. J.; AlFaraj, Y. S.; Diercks, C. S.; Jarenwattananon, N. N.; Yaghi, O. M. Conversion of Imine to Oxazole and Thiazole Linkages in Covalent Organic Frameworks. *J. Am. Chem. Soc.* **2018**, *140*, 9099–9103.
32. Haase, F.; Troschke, E.; Savasci, G.; Banerjee, T.; Duppel, V.; Dörfler, S.; Grundei, M. M. J.; Burow, A. M.; Ochsenfeld, C.; Kaskel, S.; Lotsch, B. V. Topochemical Conversion of an Imine-into a Thiazole-Linked Covalent Organic Framework Enabling Real Structure Analysis. *Nat. Commun.* **2018**, *9*, 2600.
33. Ranjeesh, K. C.; Illathvalappil, R.; Veer, S. D.; Peter, J.; Wakchaure, V. C.; Goudappagouda;Raj, K. V.; Kurungot, S.; Babu, S. S. Imidazole-Linked Crystalline Two-Dimensional Polymer with Ultrahigh Proton-Conductivity. *J. Am. Chem. Soc.* **2019**, *141*, 14950–14954.
34. Haase, F.; Lotsch, B. V. Solving the COF Trilemma: Towards Crystalline, Stable and Functional Covalent Organic Frameworks. *Chem. Soc. Rev.* **2020**, *49*, 8469–8500.
35. Zhang, G.; Xu, N.; Yang, M.; Wang, W.; Su, K.; Yuan, D. Ultrastable Imidazole-Linked Porous Organic Cages for Ammonia Capture and Detection. *Angew. Chem. Int. Ed.* **2025**, *64*, e202423226.
36. Dalapati, S.; Addicoat, M.; Jin, S.; Sakurai, T.; Gao, J.; Xu, H.; Irle, S.; Seki, S.; Jiang, D. Rational Design of Crystalline Supermicroporous Covalent Organic Frameworks with Triangular Topologies. *Nat. Commun.* **2015**, *6*, 7786.
37. Tian, Y.; Xu, S.-Q.; Liang, R.-R.; Qian, C.; Jiang, G.-F.; Zhao, X. Construction of Two Heteropore Covalent Organic Frameworks with Kagome Lattices. *Cryst. Eng. Comm.* **2017**, *19*, 4877–4881.
38. Cai, S.-L.; He, Z.-H.; Li, X.-L.; Zhang, K.; Zheng, S.-R.; Fan, J.; Liu, Y.; Zhang, W.-G. An Unprecedented 2D Covalent Organic Framework with an htb Net Topology. *Chem. Commun.* **2019**, *55*, 13454–13457.
39. Schneebeli, S. T.; Frasconi, M.; Liu, Z.; Wu, Y.; Gardner, D. M.; Strutt, N. L.; Cheng, C.; Carmieli, R.; Wasielewski, M. R.; Stoddart, J. F. Electron Sharing and Anion–π Recognition in Molecular Triangular Prisms. *Angew. Chem. Int. Ed.* **2013**, *52*, 13100–13104.
40. Mastalerz, M.; Oppel, I. M. Rational Construction of an Extrinsic Porous Molecular Crystal with an Extraordinary High Specific Surface Area. *Angew. Chem. Int. Ed.* **2012**, *51*, 5252–5255.
41. Wei, P.-F.; Qi, M.-Z.; Wang, Z.-P.; Ding, S.-Y.; Yu, W.; Liu, Q.; Wang, L.-K.; Wang, H.-Z.; An, W.-K.; Wang, W. Benzoxazole-Linked Ultrastable Covalent Organic Frameworks for Photocatalysis. *J. Am. Chem. Soc.* **2018**, *140*, 4623–4631.
42. Zhu, X.; Jia, Y.; Liu, Y.; Xu, J.; He, H.; Wang, S.; Shao, Y.; Zhai, Y.; Zhu, Y. Enhancing Built-in Electric Fields via Molecular Symmetry Modulation in Supramolecular Photocatalysts for Highly Efficient Photocatalytic Hydrogen Evolution. *Angew. Chem. Int. Ed.* **2024**, *63*, e202405962.
43. Bai, Y.; Li, C.; Liu, L.; Yamaguchi, Y.; Bahri, M.; Yang, H.; Gardner. A.; Zwijnenburg, M.; Browning, N.; Cowan, A.; Kudo, A.; Cooper, A.; Sprick, R. Photocatalytic Overall Water Splitting Under Visible Light Enabled by a Particulate Conjugated Polymer Loaded with Palladium and Iridium. *Angew. Chem. Int. Ed.* **2022**, *61*, e202201299.
44. Sachs, M.; Sprick, R.; Pearce, D.; Hillman, S.; Monti, A.; Guilbert, A.; Brownbill, N.; Dimitrov, S.; Shi, X.; Blanc, F.; Zwijnenburg, M.; Nelson, J.; Durrant, J.; Cooper, A. Understanding Structure-Activity Relationships in Linear Polymer Photocatalysts for Hydrogen Evolution. *Nat. Commun.* **2018**, *9*, 4968.
45. Yang, H.; Li, C.; Liu, T.; Fellowes T.; Chong, S.; Catalano, L.; Bahri, M.; Zhang, W.; Xu, Y.; Liu, L.; Zhao, W.; Gardner, A.; Clowes, R.; Browning, N.; Li, X.; Cowan, A.; Cooper, A. Packing-Induced Selectivity Switching in Molecular Nanoparticle Photocatalysts for Hydrogen and Hydrogen Peroxide Production. *Nat. Nanotechnol.* **2023**, *18*, 307–315.
46. Li, C.; Liu, T.; Thwaites, O.; Gardner, A.; Sazanovich, I.; Yang, H.; Li, X.; Cooper, A.; Cowan, A. Time-Resolved Vibrational Spectroscopic Study of Molecular Nanoaggregate Photocatalysts. *Chem. Sci.* **2024**, *15*, 16133–16141.
47. Wang, X.; Kafizas, A.; Li, X.; Moniz, S.; Reardon, P.; Tang, J.; Parkin, I.; Durrant, J. Transient Absorption Spectroscopy of Anatase and Rutile: The Impact of Morphology and Phase on Photocatalytic Activity. *J. Phys. Chem. C* **2015**, *119*, 10439–10447.
48. Pesci, F.; Cowan, A.; Alexander, B.; Durrant, J.; Klug, D. Charge Carrier Dynamics on Mesoporous WO_3 During Water Splitting. *J. Phys. Chem. Lett.* **2011**, *2*, 1900–1903.
49. Dong, P.; Wang, Y.; Zhang, A.; Cheng, T.; Xi, X.; Zhang, J. Platinum Single Atoms Anchored on a Covalent Organic Framework: Boosting Active Sites for Photocatalytic Hydrogen Evolution. *ACS Catal.* **2021**, *11*, 13266–13279.

Citation: *CCS Chem.* **2026**, Just Published. DOI: 10.31635/ccschem.026.202607343
Link to VoR: https://doi.org/10.31635/ccschem.026.202607343